


Cite this: *RSC Adv.*, 2020, 10, 9833

# Blow-spun N-doped carbon fiber based high performance flexible lithium ion capacitors†

Changzhen Zhan,<sup>a</sup> Jianan Song,<sup>b</sup> Xiaolong Ren,<sup>b</sup> Yang Shen,<sup>b</sup> Hui Wu,<sup>b</sup> Feiyu Kang<sup>c</sup> and Zheng-Hong Huang<sup>\*b</sup>

Constructing flexible hybrid supercapacitors is a feasible way to achieve devices with high energy density, high power density and flexibility at the same time. Herein, flexible asymmetric hybrid supercapacitors are fabricated with blow spun activated carbon fibers. Owing to the highly effective conductive network, abundant nitrogen doping, optimized pore-structure and surface chemical properties of the carbon fibers, the as-prepared flexible hybrid supercapacitor shows outstanding energy and power performance ( $98 \text{ W h kg}^{-1}$  ( $0.3 \text{ mW h cm}^{-2}$ ) @  $400 \text{ W kg}^{-1}$ ,  $9 \text{ W h kg}^{-1}$  @  $34 \text{ kW kg}^{-1}$ ), as well as excellent cycle stability with 93% capacitance retention after 4000 cycles.

Received 10th December 2019  
Accepted 24th February 2020

DOI: 10.1039/c9ra10348a

rsc.li/rsc-advances

## 1. Introduction

Energy storage devices have gradually become a research hot-spot in recent years.<sup>1,2</sup> Due to the rapid development of mobile internet and portable devices, the major demands for energy storage devices are mainly: high energy density (long endurance), high power density (fast charging) and flexibility (wearable).<sup>3–6</sup> Lithium ion batteries (LIBs) and supercapacitors are the most representative commercial energy storage devices to meet the first two requirements with energy density up to  $300 \text{ W h kg}^{-1}$  and power density up to  $10 \text{ kW kg}^{-1}$ , respectively.<sup>7</sup> As a combination of battery and supercapacitor, hybrid supercapacitors (HSCs) aim at constructing novel devices with the positive features of both batteries and supercapacitors.<sup>6,8–10</sup> In our previous work, devices with excellent performance (maximum energy density up to  $140 \text{ W h kg}^{-1}$  and  $40 \text{ W h kg}^{-1}$  at an extremely high power density of  $100 \text{ kW kg}^{-1}$ , based on active materials) were fabricated through the hybrid strategy.<sup>11,12</sup> Namely, constructing flexible HSCs (FHSCs) is a feasible way to achieve the integration of all the elements of people's needs. Carbon fibers with adjustable pore-structures are promising electrode materials for both positive electrode materials (anion absorption/de-sorption) and negative materials ( $\text{Li}^+$  storage) for HSCs. Thus, electrospun carbon fibers are widely used as the electrode materials for supercapacitors,<sup>13,14</sup>

Li-ion batteries<sup>15,16</sup> and other energy storage devices.<sup>17</sup> However, the electrospinning methodology lacks convenience, efficiency and security. In contrast, blow spinning is not only free of high voltage, but also has a several times higher production rate.<sup>18–20</sup> However, to our knowledge, there are few reports on the use of blow spun carbon fibers as the electrode material of electrochemical energy storage devices at present. Herein, as a proof of concept, blow spun polyacrylonitrile (PAN) fibers were used as precursors to obtain both the positive and negative electrode materials of HSC by means of ammonia activation and direct carbonization, respectively. Due to the superior flexibility of blow spun carbon non-woven fabrics and their optimal pore structure and surface chemical properties, FHSC coupled with blow spun carbon fibers (BSCFs) and blow spun activated carbon fibers (BSACFs) shows great energy and power performance ( $98 \text{ W h kg}^{-1}$  ( $0.3 \text{ mW h cm}^{-2}$ ) @  $400 \text{ W kg}^{-1}$ ,  $9 \text{ W h kg}^{-1}$  @  $34 \text{ kW kg}^{-1}$ ), as well as excellent cycle stability with 93% capacitance retention after 4000 cycles, indicating its great prospect in the flexible energy storage field.

## 2. Experimental

### Synthesis of BSCFs and BSACFs

10 wt% of PAN ( $\text{MW} = 1.5 \times 10^5 \text{ g mol}^{-1}$ ; Aldrich) dissolved in dimethylformamide (DMF) was loaded in a 2 ml injector with a 22-gauge needle tip. The injector tip was placed in the pipe continuously blowing air. The blow-spun fibers were collected on a piece of  $10 \times 10 \text{ cm}$  nickel. The blow-spun fibers were preoxidized during the slow temperature rise from  $200^\circ\text{C}$  to  $280^\circ\text{C}$  in 8 hours in air. Then the preoxidized fibers were heated to  $700^\circ\text{C}$  with  $5^\circ\text{C min}^{-1}$  in a tube furnace and held for 1 hour under Ar atmosphere for BSCFs and heated to  $800^\circ\text{C}$  with  $5^\circ\text{C min}^{-1}$  under Ar and held for 1 hour under ammonia atmosphere for BSACFs. Moreover, BSACFs-700 and BSACFs-

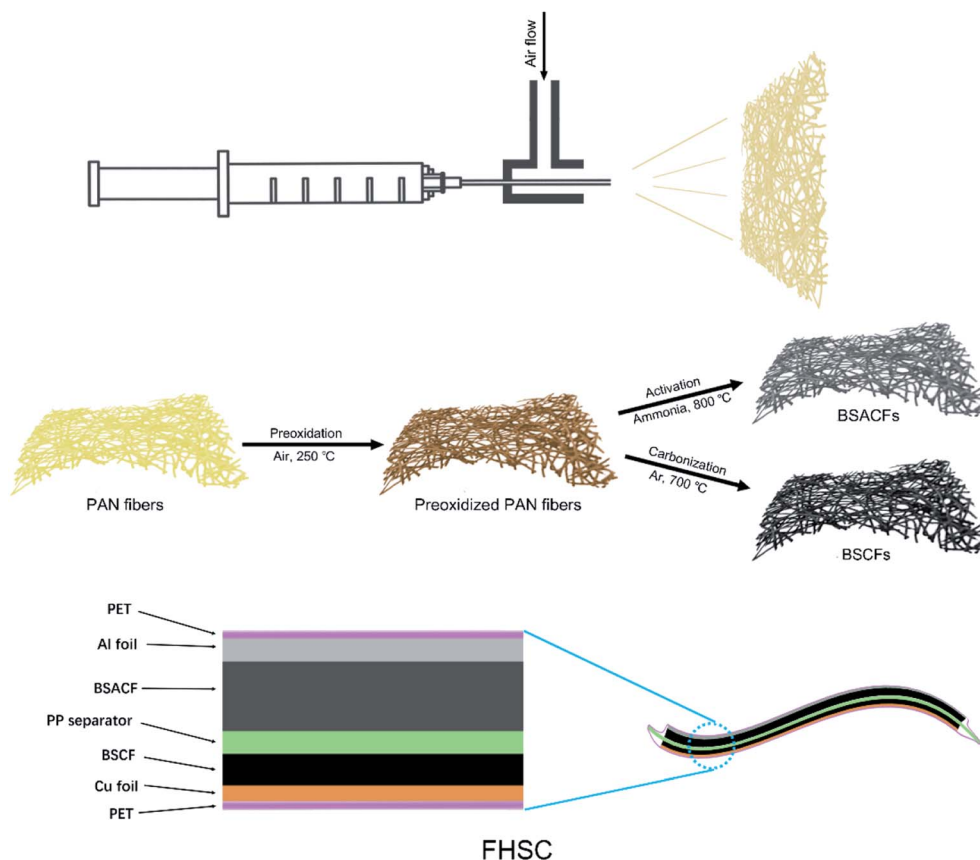
<sup>a</sup>National Institute of Clean-and-Low-Carbon Energy, P. O. Box 001, Future Science & Technology City, Changping District, Beijing, 102209, PR China

<sup>b</sup>State Key Laboratory of New Ceramics and Fine Processing, School of Materials Science and Engineering, Tsinghua University, Beijing 100084, China. E-mail: zhhuang@tsinghua.edu.cn; Fax: +86 10 62773752; Tel: +86 10 62773752

<sup>c</sup>Engineering Laboratory for Functionalized Carbon Materials, Graduate School at Shenzhen, Tsinghua University, Shenzhen 518055, China

† Electronic supplementary information (ESI) available. See DOI: 10.1039/c9ra10348a





Scheme 1 Synthesis of BSCFs and BSACFs and fabrication of FHSC.

900 were also prepared by the 1 hour ammonia activation at 700 °C and 900 °C, respectively, as contrast samples.

### Fabrication of cells

BSCFs and BSACFs fabrics were punched into disks with diameter of 12 mm for electrochemical tests. The mass loading of electrodes was about 2 mg. LIBs were assembled by using a lithium metal electrode and BSCFs/BSACFs based disk. Symmetric supercapacitors were assembled by two BSACFs electrodes. All devices were fabricated into 2032 coin cells with 1 M LiPF<sub>6</sub> electrolyte in EC/DMC (1 : 1 by volume).

### Prelithiation of BSCFs

BSCFs anode was prelithiated by galvanostatic charge/discharge process. Typically, BSCFs electrode was fabricated with Li metal in two electrodes system, and then galvanostatically discharge/charge with potential range of 3–0.01 V (vs. Li/Li<sup>+</sup>) for 5 cycles. Last, terminal potential were fixed at 0.4 V by isobarically discharge process and held for 2 h.

### Fabrication of FHSCs

4 × 4 cm BSACFs and prelithiated BSCFs infiltrated with electrolyte (1 M LiPF<sub>6</sub> electrolyte in EC/DMC) were separated with a PP film and packaged with polyethylene terephthalate (PET)

film (Scheme 1). Al foil and Cu foil with leads were also introduced into the system as current collectors for positive and negative electrode, respectively.

## 3. Results and discussion

Synthesis of BSCFs and BSACFs, together for the fabrication of flexible HSC are shown in Scheme 1. Scanning electron microscope (SEM) images of blow spun PAN fibers are shown in Fig. S1 (ESI†). The diameters of PAN fibers are evenly distributed at about 1–3 μm, which is obviously larger than electrospun fibers<sup>21</sup> and helps increase the flexibility of the non-woven fabrics. SEM images of BSCFs and BSACFs are presented in Fig. 1a and b. The morphology of the fibers remain intact and the diameters of the fibers significantly decrease due to the inevitable shrink of PAN during the carbonization and activation process.<sup>22</sup> No obvious etching effects of ammonia are observed in BSACFs, indicating the activation only affects the pore structure without destroying the morphology and mechanical property of carbon fibers. Transmission electron microscope (TEM) images of BSCFs and BSACFs shown in Fig. S2a and b† also reveal the diameter of the fibers are reduced to under 1 μm and no obvious lattice fringe are observed in the inset high resolution transmission electron microscope (HRTEM) images, suggesting the amorphous structure of BSCFs and BSACFs.<sup>23</sup>



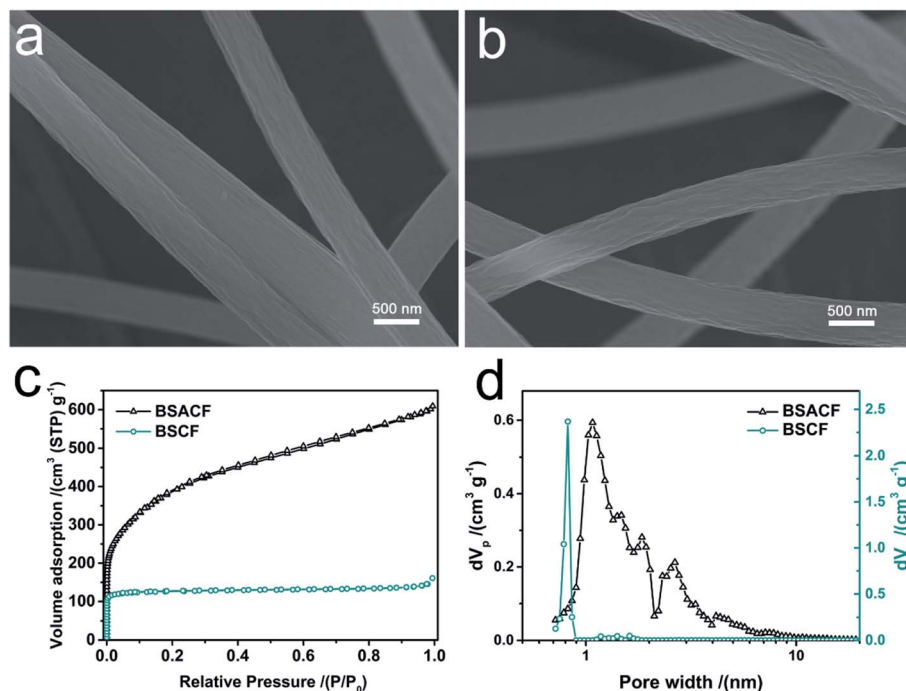


Fig. 1 SEM images of BSCFs (a) and BSACFs (b);  $N_2$  adsorption/desorption isotherms (c) of BSCFs and BSACFs and the corresponding PSD curves (d).

Such amorphous structure was further confirmed by X-ray diffraction (XRD) and Raman spectrum characterizations. XRD pattern of BSCFs and BSACFs are shown in Fig. S3.† Two broad peaks located at about  $22.8^\circ$  and  $43.8^\circ$  are attributed to the diffraction of (002) and (100) plane of graphitic layers in the amorphous carbon.<sup>19</sup> The high intensity in low angle (lower than  $20^\circ$ ) may be caused by the microporous structure of BSCFs and BSACFs.<sup>24</sup> Fig. S4† shows the Raman spectrum of BSCFs and BSACFs. Two distinct peaks centered at  $1342\text{ cm}^{-1}$  and  $1595\text{ cm}^{-1}$  can be ascribed to the D (defect)- and G (graphitic)-bands of carbon materials. The intensity ratio of D/G of BSCFs and BSACFs are both approximately 1, indicating their amorphous structure, which shows highly consistent with the HRTEM and XRD results.<sup>23</sup>

To further evaluate the texture property of BSCFs and BSACFs,  $N_2$  adsorption-desorption measurement was conducted at 77 K and the results were shown in Fig. 1c and d. Fig. 1c displays the  $N_2$  adsorption/desorption isotherms of the samples. BSCFs exhibits a type I isotherm, indicating its micropore structure.<sup>25</sup> After ammonia treatment, BSACFs shows a hybrid sorption isotherm. The amount of nitrogen adsorption increases significantly at a low relative pressure ( $P/P_0 < 0.01$ ) and nitrogen adsorption increases sustained between 0.1 and 0.9 of the  $P/P_0$  value, which can be attributed to the rapid increase of micropores and the appearance of mesopores during the activation process.<sup>25</sup> Such conclusion is further confirmed by the corresponding pore size distribution (PSD) curves displayed in Fig. 1d and specific surface area (SSA) information summarized in Table 1. BSCFs demonstrates a unimodal distribution with only micropores intensively located at about 0.8 nm and

a moderate SSA of  $409\text{ m}^2\text{ g}^{-1}$ , which could provide sufficient lithium ion adsorption sites and avoid excessive electrolyte consumption during the formation of SEI while hired as LIB anode material.<sup>26</sup> BSACFs possesses a much higher SSA of  $1412\text{ m}^2\text{ g}^{-1}$  and a multimodal distribution with micropores located at 1.0, 1.4, 1.8 nm and mesopores located at 2.6 and 4.2 nm. Such optimized hierarchical pore structure could be promising in supercapacitors applications by means of its large amounts of energy storage sites brought from micropores and high-speed ion transport path provided by mesopores.<sup>24</sup> Moreover, BSACFs-700 and BSACFs-900 were also prepared as contrasts to explore the temperature of the ammonia activation process. As shown in Table S1,† BSACFs-700 shows a much lower SSA of  $701\text{ m}^2\text{ g}^{-1}$  than BSACFs, which will lead to a much lower capacitance in the (electronic double layer capacitor) EDLC behavior [AA18]. BASCF-900 exhibits a moderate SSA of  $976\text{ m}^2\text{ g}^{-1}$ . However, due to the intense etching of ammonia under  $900^\circ\text{C}$ , the yield of BSACFs-900 is much lower than BSACFs, and the strength and flexibility of the fabrics were destroyed by over-etching of ammonia. Therefore, BSACFs (namely, BSACFs-800) was chosen

Table 1 Physicochemical properties of the samples

Samples	$S_{\text{BET}}^a$ ( $\text{m}^2\text{ g}^{-1}$ )	$V_{\text{total}}^b$ ( $\text{cm}^3\text{ g}^{-1}$ )	Elemental analysis		
			C%	O%	N%
BSCFs	409	0.248	83.99	2.91	13.1
BSACFs	1412	0.938	96.13	1.47	2.4

<sup>a</sup> Specific surface area calculated by BET method. <sup>b</sup> Total pore volume.



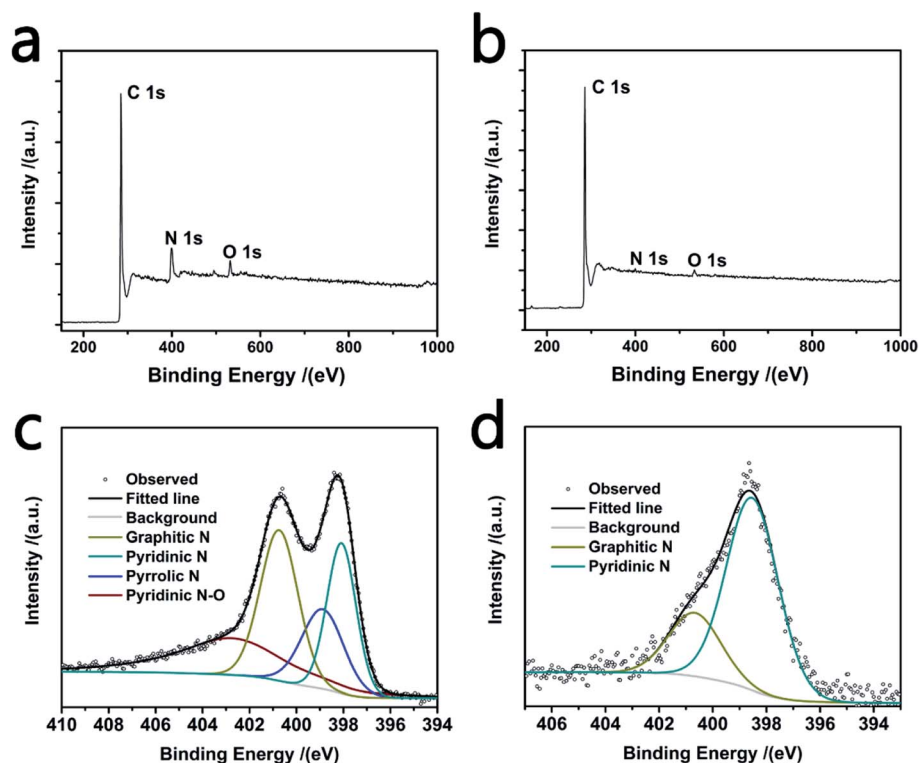


Fig. 2 XPS survey spectra of BSCFs (a) and BSACFs (b); high-resolution N 1s spectrum of BSCFs (c) and BSACFs (d).

for the subsequent measurements and fabrication of hybrid supercapacitors.

Fig. 2 presents the X-ray photoelectron spectroscopy (XPS) survey spectra of BSCFs and BSACFs, and the semi-quantitative analysis results are summarized in Table 1. BSCFs exhibits a high nitrogen content of 13.1 wt% due to the residual nitrogen in the PAN molecular chain.<sup>22</sup> BSACFs maintains a lower nitrogen content of 2.4 wt%, which is ascribed to the higher temperature heat treatment during ammonia activation. High-resolution N 1s spectrum of the carbon fibers are fitted in four component peaks and the results are shown in Fig. 2c and d. Particularly, predominant pyridinic N providing extra redox pseudocapacitance and graphitic N which could further enhance the conductivity of the carbon materials are both beneficial in lithium ions storage process and electrochemical capacitive behaviors.<sup>25</sup> Attenuated Total Internal Reflectance Fourier Transforms Infrared Spectra (ATR-FTIR) was used to investigate the surface functional groups (Fig. S5†). Two weak peaks located at  $2931\text{ cm}^{-1}$  and  $2864\text{ cm}^{-1}$  in BSCFs are ascribed to the stretching vibrations of C–H.<sup>19</sup> The peak at about  $1537\text{ cm}^{-1}$  in BSCFs and BSACFs is correspond to C–C stretching vibration. And the broad peak at  $1081\text{ cm}^{-1}$  are ascribed to the stretching vibrations of C–O and/or C–N.<sup>24</sup> The ATR-FTIR spectra shows the existence of heteroatom in BSCFs and BSACFs, which is coincident with the XPS results. Furthermore, the SEM elemental mappings of BSCFs and BSACFs are shown in Fig. S6 and S7.† The profiles of nitrogen mapping show highly coincident with the SEM images, indicating the uniform distribution of N in BSCFs and BSACFs.<sup>19</sup>

LIB was fabricated by BSCFs and lithium metal and its electrochemical properties are presented in Fig. 3a and b. Galvanostatic charge/discharge (GCD) curves of the 1st, 3rd and 10th cycles are shown in Fig. 3a. A high initial reversible capacity of  $560\text{ mA h g}^{-1}$  (60% coulombic efficiency) is observed and  $495\text{ mA h g}^{-1}$  is maintained after 10 cycles at current density of  $50\text{ mA g}^{-1}$ . Balance between capacity and initial coulombic efficiency is optimized by the moderate SSA of BSCFs.<sup>26</sup> Moreover, owing to the highly effective conductive network formed by carbon fibers and the abundant nitrogen doping, BSCFs exhibits excellent rate performance at different current density (shown in Fig. 3b). As the current density gradually increases to  $5\text{ A g}^{-1}$ , BSCFs still maintain a quite high capacity of over  $200\text{ mA h g}^{-1}$ . Low potential range and outstanding rate performance indicate its great prospect in anode materials of lithium ion hybrid supercapacitor.<sup>11</sup>

Symmetric supercapacitor (SC) was fabricated by BSACFs and its electrochemical properties are presented in Fig. 3c and d. GCD curves under different current density from  $0.1\text{ A g}^{-1}$  to  $2\text{ A g}^{-1}$  show well shaped isosceles triangle shapes and negligible IR drops, indicating good EDLC behavior and high conductivity of BSACFs.<sup>24</sup> BSACFs based SC exhibits a high specific capacitance of  $130\text{ F g}^{-1}$  at current density of  $0.1\text{ A g}^{-1}$ , which is associated with large SSA provided by the abundant micropores.<sup>27</sup> And a high capacitance of  $74\text{ F g}^{-1}$  is obtained at a high current density of  $10\text{ A g}^{-1}$ , confirming its good rate performance.

FHSC was fabricated by coupling BSACFs and prelithiated BSCFs with  $1\text{ M LiPF}_6$  electrolyte (photos shown in Fig. S8†).





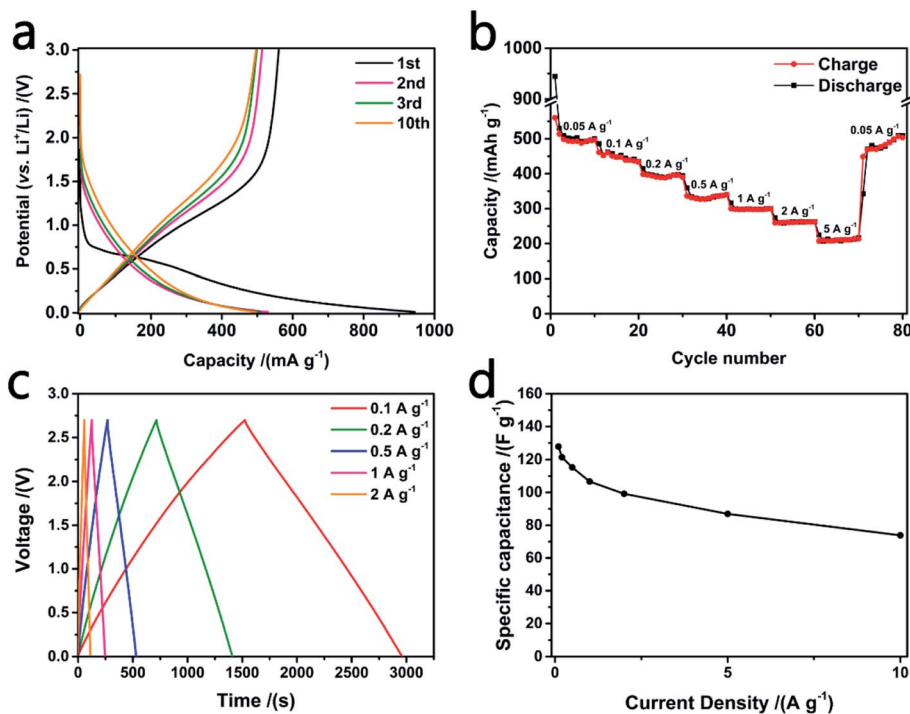


Fig. 3 (a) GCD curves of the 1st, 3rd and 10th cycles of BSCFs based LIB; (b) rate performance of BSCFs based LIB. (c) GCD curves of BSACFs based SC under different current density from  $0.1 \text{ A g}^{-1}$  to  $2 \text{ A g}^{-1}$ ; (d) rate performance of BSACFs based SC.

According to the GCD curve of BSCFs in a high potential range of 1.5–4.6 V (shown in Fig. S9†), BSACFs shows liner shape GCD curve (corresponding ions absorption/de-sorption) at potential

between 2 V and 4.6 V. BSCFs stores  $\text{Li}^+$  at the potential range of about 0 to 0.4 V (pre-lithiation potential). Therefore, the voltage window of the as-fabricated FHSC was fitted at 1.5 V to 4.5 V in

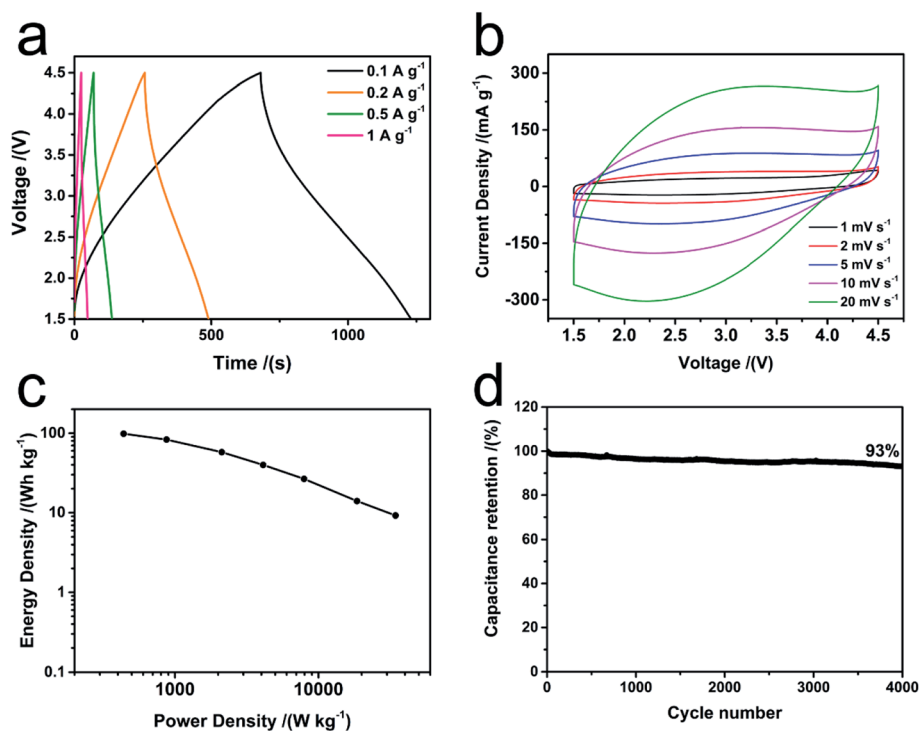


Fig. 4 (a) GCD curves of BSACFs/BSCFs FHSC at different current density from  $0.1 \text{ A g}^{-1}$  to  $1 \text{ A g}^{-1}$ ; (b) CV curves of FHSC at different sweep rates from  $1 \text{ mV s}^{-1}$  to  $20 \text{ mV s}^{-1}$ ; Ragone plots (c) and cycle performance (d) of FHSC.

the following electrochemical measurements. Mass ratio of two electrodes was carefully discussed (Fig. S10†) and fitted at  $m_{\text{BSCFs}} : m_{\text{BSACFs}} = 1 : 3$ . Fig. 4a exhibits the GCD curves of BSACFs//BSCFs FHSC at different current density from 0.1 A g<sup>-1</sup> to 1 A g<sup>-1</sup>. GCD curves exhibit nearly linear shapes and no obvious polarization is observed, revealing the capacitive behaviors of as-prepared FHSC. Cyclic voltammetry (CV) was performed and the results are shown in Fig. 4b. Quasi-rectangular shaped curves are observed, demonstrating the capacitive predominant mechanism, which is highly agreed with the GCD results. As the scan rate gradually increases from 1 mV s<sup>-1</sup> to 20 mV s<sup>-1</sup>, the curves maintain the rectangular shape, indicating the good rate performance of FHSC. Ragone plots with energy density and power density are summarized in Fig. 4c. FHSC presents a high energy density of 98 W h kg<sup>-1</sup> (0.3 mW cm<sup>-2</sup>, areal density 3 mg cm<sup>-2</sup>, based on mass of active materials) at power density of 400 W kg<sup>-1</sup>. Such high energy of FHSC is attributed to the abundant ions adsorption sites brought by numerous micropores of BSACFs and the high lithium ion storage capacity of BSCFs. Due to the good conductive network, optimized pore structure and effective N doping, as-fabricated FHSC exhibits superior power density of maintaining 9 W h kg<sup>-1</sup> at 34 kW kg<sup>-1</sup>. Moreover, as shown in Fig. 4d, as-fabricated FHSC also exhibits an excellent cycle stability with 93% capacitance retention after 4000 cycles. And the observed energy density, power density and cycle stability of the BSCFs//BSACFs FHSC is superior to most of the other flexible hybrid capacitors<sup>28–32</sup> (as compared in Table S2†).

## 4. Conclusions

In summary, a FHSC was fabricated with blow spun N-doped carbon fiber non-woven fabrics. BSACFs prepared by the activation of blow spun fibers exhibit superior EDLC behavior due to their optimized hierarchical pore structure and conductive network. BSCFs prepared by the direct carbonization of blow spun fibers show great performance for LIB anode materials due to the moderate SSA and the abundant nitrogen doping. Moreover, both BASCFs and BSCFs maintained good flexibility after the carbonization and activation process. Finally, the as-prepared FHSC shows outstanding energy density, power density and cycle stability (98 W h kg<sup>-1</sup> (0.3 mW h cm<sup>-2</sup>) @ 400 W kg<sup>-1</sup>, 9 W h kg<sup>-1</sup> @ 34 kW kg<sup>-1</sup>, 93% capacitance retention after 4000 cycles). Such superior performance shows great prospects in the flexible energy storage field and this work shows a good example of constructing flexible energy storage devices with the hybrid asymmetric battery-capacitor design.

## Conflicts of interest

There are no conflicts of interest to declare.

## Acknowledgements

This work was supported by the National Natural Science Foundation of China (grant no. 51672151) and Beijing Natural Science Foundation (no. 3162017).

## References

- 1 M. A. Hannan, M. M. Hoque, A. Mohamed and A. Ayob, Review of energy storage systems for electric vehicle applications: issues and challenges, *Renewable Sustainable Energy Rev.*, 2017, **69**, 771–789.
- 2 J. H. Won, H. M. Jeong and J. K. Kang, Synthesis of Nitrogen-Rich Nanotubes with Internal Compartments having Open Mesoporous Channels and Utilization to Hybrid Full-Cell Capacitors Enabling High Energy and Power Densities over Robust Cycle Life, *Adv. Energy Mater.*, 2017, **7**, 1601355.
- 3 W. Liu, M.-S. Song, B. Kong and Y. Cui, Flexible and Stretchable Energy Storage: Recent Advances and Future Perspectives, *Adv. Mater.*, 2017, **29**, 1603436.
- 4 M. R. Lukatskaya, B. Dunn and Y. Gogotsi, Multidimensional materials and device architectures for future hybrid energy storage, *Nat. Commun.*, 2016, **7**, 12647.
- 5 P. Yang and W. Mai, Flexible solid-state electrochemical supercapacitors, *Nano Energy*, 2014, **8**, 274–290.
- 6 J. Ding, H. Wang, Z. Li, K. Cui, D. Karpuzov, X. Tan, *et al.*, Peanut shell hybrid sodium ion capacitor with extreme energy–power rivals lithium ion capacitors, *Energy Environ. Sci.*, 2015, **8**, 941–955.
- 7 B. Dunn, H. Kamath and J.-M. Tarascon, Electrical Energy Storage for the Grid: A Battery of Choices, *Science*, 2011, **334**, 928–935.
- 8 H. Wang, C. Zhu, D. Chao, Q. Yan and H. J. Fan, Nonaqueous Hybrid Lithium-Ion and Sodium-Ion Capacitors, *Adv. Mater.*, 2017, **29**, 1702093.
- 9 Y. Lei, Z.-H. Huang, Y. Yang, W. Shen, Y. Zheng, H. Sun, *et al.*, Porous mesocarbon microbeads with graphitic shells: constructing a high-rate, high-capacity cathode for hybrid supercapacitor, *Sci. Rep.*, 2013, **3**, 2477.
- 10 E. Lim, C. Jo, M. S. Kim, M.-H. Kim, J. Chun, H. Kim, *et al.*, High-Performance Sodium-Ion Hybrid Supercapacitor Based on Nb<sub>2</sub>O<sub>5</sub>@Carbon Core-Shell Nanoparticles and Reduced Graphene Oxide Nanocomposites, *Adv. Funct. Mater.*, 2016, **26**, 3711–3719.
- 11 C. Zhan, W. Liu, M. Hu, Q. Liang, X. Yu, Y. Shen, *et al.*, High-performance sodium-ion hybrid capacitors based on an interlayer-expanded MoS<sub>2</sub>/rGO composite: surpassing the performance of lithium-ion capacitors in a uniform system, *NPG Asia Mater.*, 2018, **10**, 775–787.
- 12 X. Yu, C. Zhan, R. Lv, Y. Bai, Y. Lin, Z.-H. Huang, *et al.*, Ultrahigh-rate and high-density lithium-ion capacitors through hybridizing nitrogen-enriched hierarchical porous carbon cathode with prelithiated microcrystalline graphite anode, *Nano Energy*, 2015, **15**, 43–53.
- 13 X. Liu, M. N. Marlow, S. J. Cooper, B. Song, X. Chen, N. P. Brandon, *et al.*, Flexible all-fiber electrospun supercapacitor, *J. Power Sources*, 2018, **384**, 264–269.
- 14 X. Lu, C. Wang, F. Favier and N. Pinna, Electrospun nanomaterials for supercapacitor electrodes: designed architectures and electrochemical performance, *Adv. Energy Mater.*, 2017, **7**, 1601301.



- 15 F. Pantò, Y. Fan, S. Stelitano, E. Fazio, S. Patané, P. Frontera, *et al.*, Electrospun C/GeO<sub>2</sub> paper-like electrodes for flexible Li-ion batteries, *Int. J. Hydrogen Energy*, 2017, **42**, 28102–28112.
- 16 X. Liu, Y. Jiang, K. Li, F. Xu, P. Zhang and Y. Ding, Electrospun free-standing N-doped C@ SnO<sub>2</sub> anode paper for flexible Li-ion batteries, *Mater. Res. Bull.*, 2019, **109**, 41–48.
- 17 X. Mao, T. A. Hatton and G. C. Rutledge, A review of electrospun carbon fibers as electrode materials for energy storage, *Curr. Org. Chem.*, 2013, **17**, 1390–1401.
- 18 E. S. Medeiros, G. M. Glenn, A. P. Klamczynski, W. J. Orts and L. H. Mattoso, Solution blow spinning: a new method to produce micro-and nanofibers from polymer solutions, *J. Appl. Polym. Sci.*, 2009, **113**, 2322–2330.
- 19 K. Wang, N. Zhao, S. Lei, R. Yan, X. Tian, J. Wang, *et al.*, Promising biomass-based activated carbons derived from willow catkins for high performance supercapacitors, *Electrochim. Acta*, 2015, **166**, 1–11.
- 20 M. Hu, H. Zhou, X. Gan, L. Yang, Z. H. Huang, D. W. Wang, *et al.*, Ultrahigh rate sodium ion storage with nitrogen-doped expanded graphite oxide in ether-based electrolyte, *J. Mater. Chem. A*, 2018, **6**, 1582–1589.
- 21 Y. Bai, Z.-H. Huang, X. Yu, K. Kaneko and F. Kang, Micro-mesoporous graphitic carbon nanofiber membranes, *Carbon*, 2018, **132**, 746–748.
- 22 C. Zhan, Q. Xu, X. Yu, Q. Liang, Y. Bai, Z.-H. Huang, *et al.*, Nitrogen-rich hierarchical porous hollow carbon nanofibers for high-performance supercapacitor electrodes, *RSC Adv.*, 2016, **6**, 41473–41476.
- 23 X. Gao, C. Zhan, X. Yu, Q. Liang, R. Lv, G. Gai, *et al.*, A High Performance Lithium-Ion Capacitor with Both Electrodes Prepared from Sri Lanka Graphite Ore, *Materials*, 2017, **10**, 414.
- 24 Q. Liang, L. Ye, Z.-H. Huang, Q. Xu, Y. Bai, F. Kang, *et al.*, A honeycomb-like porous carbon derived from pomelo peel for use in high-performance supercapacitors, *Nanoscale*, 2014, **6**, 13831–13837.
- 25 C. Zhan, X. Yu, Q. Liang, W. Liu, Y. Wang, R. Lv, *et al.*, Flour food waste derived activated carbon for high-performance supercapacitors, *RSC Adv.*, 2016, **6**, 89391–89396.
- 26 D. Nan, Z.-H. Huang, F.-Y. Kang and W.-C. Shen, Electrospun N-doped porous carbon nanofiber webs as anodes for lithium-ion batteries, *Carbon*, 2016, **110**, 521.
- 27 X. Yu, J. Lu, C. Zhan, R. Lv, Q. Liang, Z.-H. Huang, *et al.*, Synthesis of activated carbon nanospheres with hierarchical porous structure for high volumetric performance supercapacitors, *Electrochim. Acta*, 2015, **182**, 908–916.
- 28 B. Deng, T. Lei, W. Zhu, L. Xiao and J. Liu, In-plane assembled orthorhombic Nb<sub>2</sub>O<sub>5</sub> nanorod films with high-rate Li<sup>+</sup> intercalation for high-performance flexible Li-ion capacitors, *Adv. Funct. Mater.*, 2018, **28**, 1704330.
- 29 H. Wang, C. Guan, X. Wang and H. J. Fan, A high energy and power Li-ion capacitor based on a TiO<sub>2</sub> nanobelt array anode and a graphene hydrogel cathode, *Small*, 2015, **11**, 1470–1477.
- 30 H. Li, L. Peng, Y. Zhu, X. Zhang and G. Yu, Achieving high-energy-high-power density in a flexible quasi-solid-state sodium ion capacitor, *Nano Lett.*, 2016, **16**, 5938–5943.
- 31 Q. Yang, S. Cui, Y. Ge, Z. Tang, Z. Liu, H. Li, *et al.*, Porous single-crystal NaTi<sub>2</sub>(PO<sub>4</sub>)<sub>3</sub> via liquid transformation of TiO<sub>2</sub> nanosheets for flexible aqueous Na-ion capacitor, *Nano Energy*, 2018, **50**, 623–631.
- 32 S. Dong, H. Li, J. Wang, X. Zhang and X. Ji, Improved flexible Li-ion hybrid capacitors: techniques for superior stability, *Nano Res.*, 2017, **10**, 4448–4456.

